The Thesis Committee for Raul David Montaño
Certifies that this is the approved version of the following Thesis:

Optical Measurements of the Thermodynamic Response in Graphite due to Extreme Strain

APPROVED BY
SUPERVISING COMMITTEE:

Yaguo Wang, Supervisor

Vaibhav Bahadur

Optical Measurements of the Thermodynamic Response in Graphite due to Extreme Strain

by

Raul David Montaño

Thesis

Presented to the Faculty of the Graduate School of

The University of Texas at Austin

in Partial Fulfillment

of the Requirements

for the Degree of

Master of Science in Mechanical Engineering

The University of Texas at Austin

May 2021

Dedication

To my parents, who have taught me all that I know and inspire all that I strive to be.

Acknowledgements

I would like to begin by extending my gratitude to my advisor, Professor Yaguo Wang. Not only have you shown support and given me proper direction in testing exciting research topics but supporting my well-being outside of the lab. I am honored to be an alumna of your research group.

I also wish to thank Dr. Michael Pettes who introduced me to scientific research and has only set me up for success. Being a part of your research group on both ends of the country and the mentorship you have provided me over the years is something that I hold with great esteem.

Thank you to each of my current and previous lab mates: Sanghyeok, Jihoon, Yongjian, Zefang, Xianghai, and Jaewoo. All of whom have not only helped me in this work but whos friendships are one that I am proud to have.

Thank you to both Professor Afu Lin and Yanyao for giving me the resources to perform these experiments and knowledge to perform them successfully.

Lastly, thank you to my family whose endless support, no matter the decision or circumstance, has given me the drive to always move forward. Thank you to my mother for teaching me how to handle challenges in life and my father for teaching me to approach them with total dedication. Thank you to my sister for having my back in both the good and bad and to my brother who can always put a smile on my face.

To all the names I could not list here, thank you. This degree could not have been done without the support of all.

Abstract

Optical Measurements of the Thermodynamic Response in Graphite due to Extreme Strain

Raul David Montaño, M.S.E.

The University of Texas at Austin, 2021

Supervisor: Yaguo Wang

Upon the discovery of graphene by micromechanical exfoliation, a boom in the microelectronics community has taken place. Contrasting to their bulk counterparts, two dimensional (2D) materials are held together in layered order with weak van der Waals (vdW) forces and strongly in-plane with covalent bonds. This wide range of emerging materials have been enthusiastically researched as they can possess unique band gaps, favorable to the semiconductor industry for emerging technologies in MEMS design. In relation to the weak interlayer bonds holding new materials together, they act differently in the cross- and in-plane directions with respect to their thermal and electrical performance. These intrinsic 2D material properties can further be enhanced by external factors such as temperature, electric, and magnetic fields. Vast efforts in the scientific community have proved large developments in using strain to control optical, thermal, and electronic properties of semiconductors, acting with higher performance compared to their bulk crystal forms. In this work, a diamond anvil cell (DAC) was implemented to impose a large compressive strain on a thin graphite film in order to induce strong

interlayer covalent bonds. Measured with picosecond transient thermoreflectance (ps-TTR), an increase in cross-plane thermal conductivity ($\kappa_{\perp}$) was observed to be ~180% with strains up to ~20 GPa. Furthermore, Raman spectroscopy was employed to monitor a phase transformation from graphite into a quasi-diamond film as a shift in the G/2D graphite peaks indicated a change in material structure.

Table of Contents

List of Figures

Chapter 1: Introduction

1.1 Global Energy Consumption and Graphite

The global demand for energy steadily increases each year with growing populations and modern technological demands. In 2020, the United States of America alone produced 92.9 quads (~29 trillion kilowatt-hours) of energy to supply its citizens [1]. This mega-scale production is far too high with respect to the environmental impacts caused as ~62% of this energy is wasted and unusable. Coal, natural gas, and petroleum are traditionally the largest producers of energy in this country and still remains to be true despite low efficiencies. The flow chart below illustrates this and also highlights the lack of renewable methodology. These modern energy manufacturing processes are all grounded in material science but still require a deeper understanding from an engineering standpoint in order to be more efficient and scaled up.

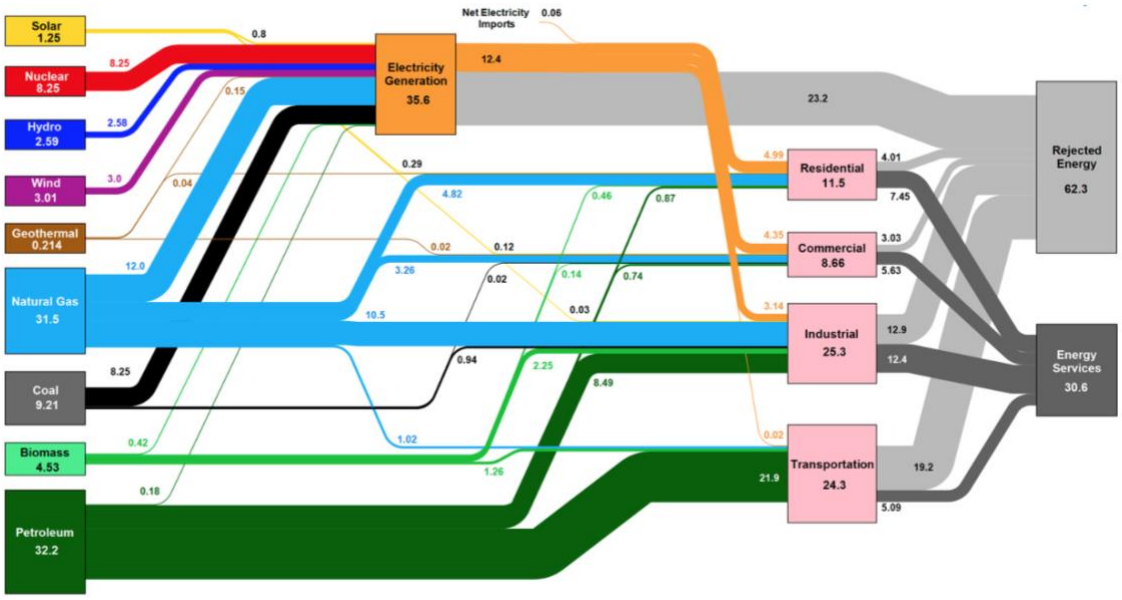

Figure 1.1: Energy production flow chart for the United States in 2021.

As the race for renewable energy production continues on, new material structures and chemical compositions must be explored to optimize current state of the art processes. Materials have intrinsic properties that often change drastically when atomically thin [2]. These material quantities vary from being physical, structural or chemical and have been studied extensively since the dawn of materials science. A wide range of which now have been measured and categorized with unique band structures: metals [3, 4], superconductors [5], wide-gap insulators [6], semiconductors [7], topological insulators [8], ferromagnets [9-10], and quantum spin Hall insulators [11]. These unique films can be layered in order to build nano devices as heterostructures built of layered two dimensional (2D) crystals have garnered a large following from researchers ever since the early 2010's [12]. These layers of 2D films are held together with forceful in-plane covalent bonds and when stacked are held with weak interlayer van der Waals (vdW) interactions out-of-plane.

In modern scientific research, graphite (and subsequently graphene) has been a key substance with revolutionary implications in flexible electronics [13], clean energy [14], and more. Graphite in itself has been extensively studied and the identification of a highly lamellar structure in graphite oxide by Benjamin Collins Brodie in 1859 [14, 15] sparked the search for graphene. The graphitic structure was identified by X-ray powder diffraction in 1916 [15] and later understood by single-crystal diffraction in 1924 [17]. About a century later, theoretical models explored the viability of graphene [18] and finally, it was produced and identified in 2004.

Graphite is a crystalline form of carbon atoms in a hexagonal structure [19]. Carbon in itself can form many allotropes in solid form, the two most common being diamond and graphite. In diamond, there are sp^3 chemical bonds in tetrahedra with each carbon atom having four nearest neighbors. In graphite there are sp^2 hybrid orbitals in

sheets with each carbon atom having three nearest neighbors separated 120 degrees apart [20, 21]. In graphene, carbon atoms are arranged in a honeycomb lattice with a bond length of 0.142 nm. Accordingly, layers in graphene are held together with van der Waals forces with a separation distance of 0.335 nm. Delving further into the anisotropic [22] structural identity of graphene, we find that these weak out-of-plane vdW bonds are supplemented by three in-plane covalent bonds with a vacant fourth bonding potential available [23]. This allows this material to have unique abilities, such as the ability to easily shear and remove layers into a highly manipulative thin sample. The aforementioned intrinsic electronic properties allow for a high in-plane electrical conductivity but a much lower (on the order of 1000 times) out-of-plane performance. Summarizing, graphene is favorable for thin device applications as it has a high current density and carrier mobility. The limiting factor, which requires further understanding of the material physics as a whole, is the nonexistence of a band gap which is required for the semiconductor industry as it acts as a switch in optical devices.

1.2 Strain Engineering of Thin Materials

High performance devices to solve some of these aforementioned issues are increasingly in demand leading researchers to find new architectures to meet these needs. The constraining factor here lies in material selection as intrinsic properties of materials have limitations in their performance in specific device criterions for optimal functionality. This drives a fork in the road of research; scientists can either explore new materials and measure their operational properties or amplify the performance of existing materials. This work explores the second case where strides have been made in surface functionalization [24, 25], defect engineering [26-28], chemical intercalation [29-31] and doping reactions [32, 33].

Naturally, thin materials are flexible and can easily have dictated strain applied in comparison to their bulk counterparts. Researchers have found that applying strain on a thin substance can significantly modify the intrinsic electronic and thermal properties of many materials. Remarkable strides have been made studying both theoretical [34, 35] and experimental [36, 37] strain tuning of a large array of materials significant to the semiconductor industry, such as black phosphorus, WSe_2, and MoS_2. There are vast methodologies to imposing strain on a material but can be summarized as four major techniques.

1.2.1 Deformation of Flexible Substrates

This method of imposing strain on a 2D material begins by placing the sample on a flexible substrate, such as polymethyl methacrylate (PMMA) or polydimethylsiloxane (PDMS). This is then attached to a high precision strain device that can either bend or strain the substrate, which is quantified be either the elongation or radius of curvature of the substrate. In stretching, strain is quantified by the simple equation $\varepsilon = \Delta L/L_0$, where L_0 is the unstretched length of the substrate, and ΔL is the change in that length [38]. Subsequently for bending, it can be measured as $\varepsilon = t/2r$, where t is combined sample and substrate thickness, and r is radius of curvature. This setup has a critical assumption in that the radius of curvature when bending must be larger than that of the substrate thickness [39]. Bending is advantageous in that it allows for strain applied in both directions, tensile or strained, based on whether the sample is placed on the top or bottom surface of the substrate.

1.2.2 Piezoelectric Substrate Actuation

The principle of piezoelectricity can be used to apply stress upon stress a material. These types of experiments employ uniquely designed substrates, such as the popular $(1-x)\left[\mathrm{Pb}(\mathrm{Mg}_{\frac{1}{3}}\mathrm{Nb}_{\frac{2}{3}})\mathrm{O}_3\right]-x[\mathrm{PbTiO}_3]$ (PMN-PT), for strain tuning of materials [40]. Here, continuous voltage can be applied and the material in question can continuously be bent, resulting with in-situ measurements. This happens as a bias voltage applied to the substrate causes an out-of-plane electric field to be generated and bends the substrate to provide either compressive or tensile strain. This type of experimentation has a drawback in that it has large power requirements to produce ample strain, listed by one study calling for 500 V for only 0.2% strain [41].

1.2.3 Atomic Force Microscopy (AFM)

The tip of an AFM can be used to impose strain on a 2D film, usually attached to researcher-designed fabricated devices, for measuring specific properties of material change. It is common for a suspended film to be measured for an electro- or thermodynamic change or tested to find mechanical limitations, such as the Young's modulus. Due to the nature of AFM operation and low throughput capabilities, these methods are not generally practical for modern devices [42].

1.2.4 Pressurized Blisters

This method entails placing a thin sample over a substrate that has an embedded microcavities. The sample creates a seal over a cavity because 2D materials intrinsically have a high order of gas molecular impermeability. Once set, an environmental change in the external pressure can be placed, leaving a difference of pressure inside the cavity. This forces films to bend and thus transfer biaxial tensile strain to the sample [43].

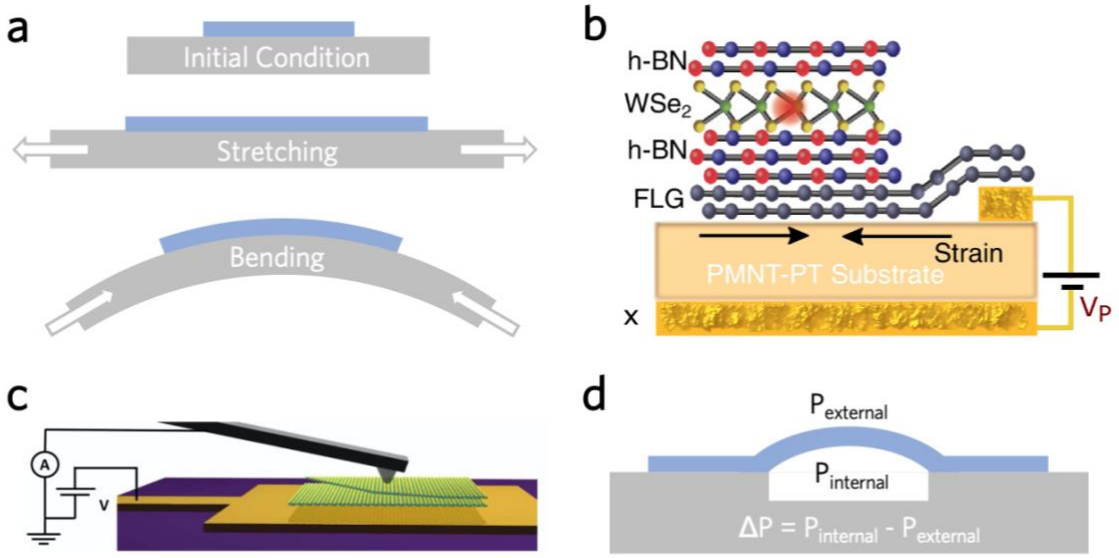

Figure 1.2: Experimental schematics for strain tuning of materials depicting a) deformation of flexible substrates, b) piezoelectric substrate actuation, c) AFM tip probing, and d) pressurized blisters.

1.3 High Pressure Physics and the Diamond Anvil Cell

The major drawback to the aforementioned methods of applying strain to materials is that only less than 3% strain can be achieved [44, 45]. In the field of geological sciences, diamond anvil cells (DAC) are commonly used to generate high pressure environments simulating deep earth environments. Traditionally, DACs are used to understand material synthesis and properties that exist outside of the surface environments we are accustomed to. These instruments use hydrostatic pressure capable of imposing compressive strain on a material by as much as 30% [46, 47]. A standard DAC may vary in specific components but has four major parts – (1) the force generating mechanism, (2) two diamonds, (3) a gasket, and (4) a pressure transmitting medium (PTM). Force is generated here uniaxially with four screws but has also been done with a

lever arm or pneumatically. Diamonds are used as the optical window as they are very hard and can endure high pressure. Along with this, they are optically clear at certain electromagnetic wavelengths allowing for a multitude of possible measurements such as Raman spectroscopy, X-ray diffraction crystallography, photoluminescence, etcetera [48]. The gasket creates a chamber between the diamonds of which samples are placed. Usually, it is a stiff metal such as rhenium or tungsten. The diameter of the chamber created by the alignment of the diamonds and gasket is generally very small, on the order of several hundred microns. This is key in generating large compressive strains through the PTM with modest applied force. In order to aid in visualizing this, the definition of pressure can be expressed as $P = F/A$, where P is pressure, F is force, and A is area. From this, we see that large forces are not needed to produce an extreme environment so long as the diamond culet diameter is small.

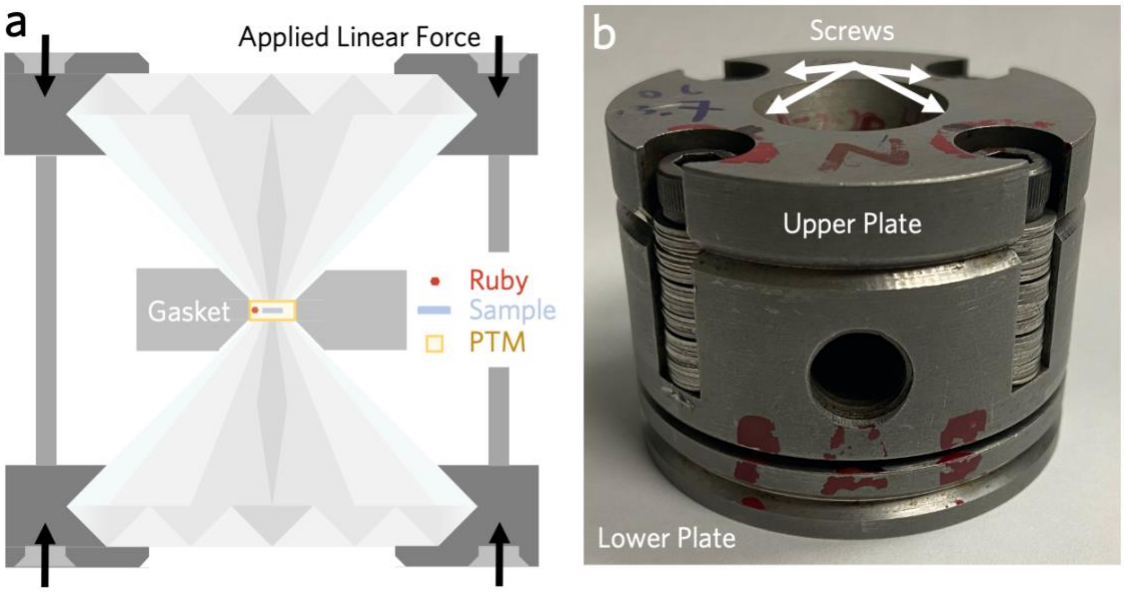

Figure 1.3: a) Illustration of a typical DAC and its components, and b) an optical image of the one used in this research study.

PTM selection can vary greatly based on the experimental constraints and can be in solid, liquid, or gaseous forms. Generally, material properties such as insulation and transparency to light need to be considered. PTMs that are in either solid (KBr, NaCl) or liquid (4:1 methanol/ethanol) form are normally the simplest to load into the DAC chamber. Media in these states of matter have a comparatively low hydrostatic limit, this restriction creates the problem in that not all materials (Al_2O_3, MgO) are suitable for pure hydrostatic pressure and can cause experimental distortions. PTMs in gaseous form (usually noble He, Ne, or Ar) are selected for use in room and low temperature investigations for their stability in the chamber. The challenge of using these proves to be difficult as specialized gas loading equipment is required.

Monitoring pressure inside the DAC can be done either optically, or by way of x-ray diffraction. In the case of x-ray pressure scaling, sodium chloride (NaCl), platinum (Pt), or gold (Au) are commonly used within the scientific community. Here, the diffraction data is taken off these materials after pressure is applied and compared to its ambient equation of state to obtain pressure values. For optical pressure tracking, florescence peak shifts are measured of a control material inside of the DAC. Rubies are commonly used but can be substituted for a samarium doped yttrium aluminum garnet (Sm:YAG) at ultra-high pressure. This is due to the fact that a ruby has a significant temperature coefficient (0.068 Å/deg) and a thermal line overlap at high pressure causing distinct florescence signatures to blend. In the case of the former, the ruby R_1 peak is characterized and used in calculation with the equation below.

$$P = \frac{A}{B}\left\{\left[1 + \frac{\Delta\lambda}{\lambda}\right]^{B} - 1\right\} \tag{1.1}$$

Where, A and B are coefficients, and $\lambda_0 = 694.22$ nm at room temperature and pressure [49, 50].

Applying hydrostatic compression with a DAC has a great advantage in that it is very consistent in applying strain on the sample. Using the aforementioned mechanical methodologies, it is not guaranteed that strain transfer between the sample and substrate interface is perfect. This is a major assumption is made in current literature studies even though slippage and nonperfect adhesion is likely. Therefore, extremely thin mono- and bilayer samples are typically used in these traditional approaches as strain transfer across layer-to-layer interfaces are not effective due to weak vdW forces holding material layers together. This causes inconsistency in experimental schemes as large uncertainties are then present in estimated the applied strain across samples. Considering the benefits of the DAC, utilizing this instrument is a convenient way of examining the strain effects on materials with high accuracy though it does have one major drawback. Here, only compressive strain can be applied on a sample whereas tensile strain has been shown to enhance material properties [51, 52] for their own varying applications.

Chapter 2: Hypothesis

Intrinsically, graphene and thin graphite are mailable materials that can be systematically engineered for physical property enhancement. Chemical reactions, such as hydrogenation [53, 54], fluorination [55-57], oxidation [58], and the intercalation of active chemical species [59] have been previously reported. Transformation is not limited here, however, looking into the layered structure of the substance opens a wide range of experimentation that has yet to be explored. Atomically thin layers of graphene are held together via weak vdW forces of which can be changed when strain is applied. When taken advantage of, thin multilayer samples can have strain applied to them inducing a stronger, covalent interlayer bonds. The undergone phase transition of thin graphitic materials in this instance can debatably be stated to be a new allotrope species of carbon. This forms an entirely new material, an uncommonly explored quasi-diamond type film. This newly synthesized material has been referred to largely as diamane, following an analogous graphene-graphane etymology popularly used now among the semiconductor industry. Fundamentally, graphene is a zero-band gap material with a free corridor between the valence and conduction band, better known as the Dirac point [60]. Graphitic films that have undergone this aforementioned phase transformation have been shown to act as a semiconductor with a band gap widening as a function of sample thickness.

The stability and transition to diamond-like graphene films is not well understood in theoretical models and has yet to be comprehensively explored in a laboratory setting. Theoretical simulations have been studied for the bulk graphite to diamond transition [61-63], alluding to interesting physical enhancements that have yet to be explored experimentally. In monoatomic graphene sheets, hydrogenation on both sides of the

single layer have been shown to be thermodynamically stable [64, 65]. When undergone this process, graphene (CH) is formed where every carbon atom, yielding sp^3-hybrid orbital states leading to an electronic bandgap as large as natural diamond. For specimens larger in thickness, however, surface chemistry cannot be the route taken to view these same results.

Logically, forcing the interlayer distance closer together in bulk graphene layers can produce the same principal results. At extremely high pressures, the interlayer distances between sheets shrink and as a result, atomic stacking order must change. Upon closer distances in carbon nearest-neighbor atoms, the previous vdW forces reinvent into much stronger covalent bonds.

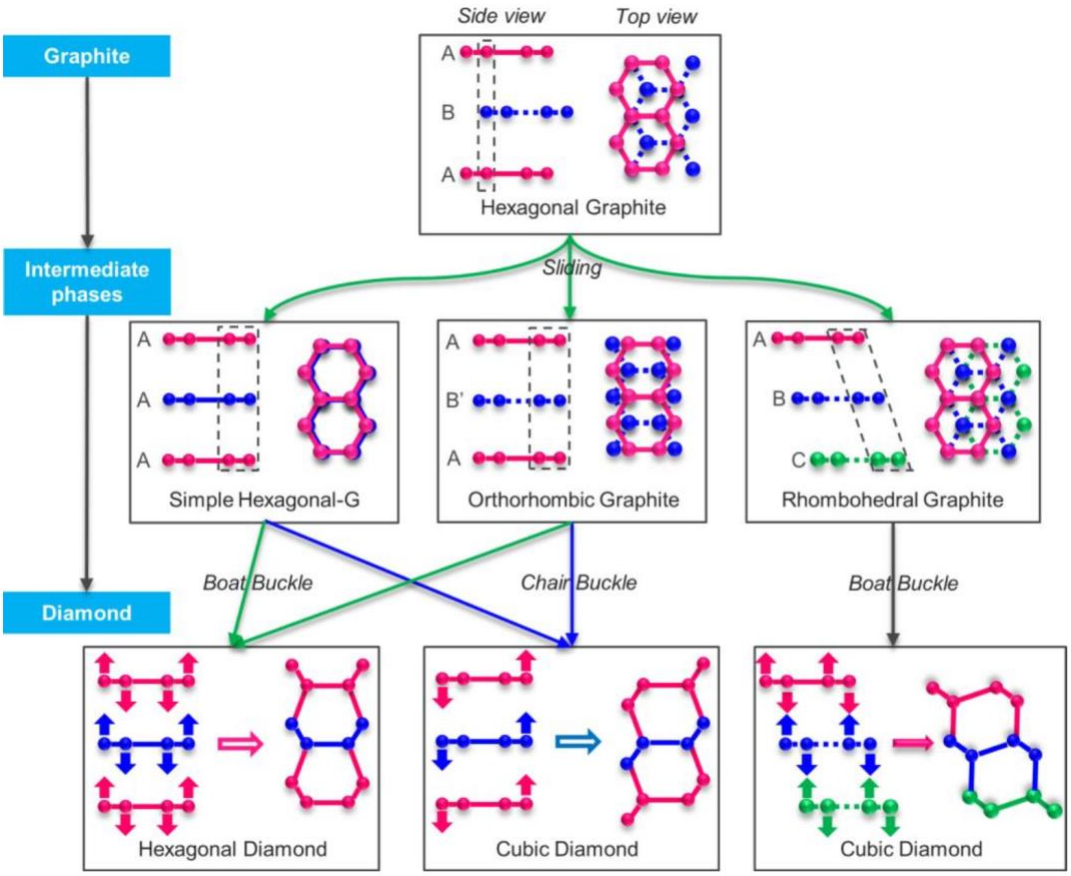

Figure 2.1: Stacking order routes of the phase transformation of graphite to quasi-diamond films [66].

This work seeks to bridge the gap in theorized models and experimental observations that have yet to be reported. Therefore, imposing extreme compressive strain on thin, non-specifically ordered graphite, a phase transition to a diamond-like film will induce local electronic orbital hybridization of order sp^3 leading to a thermodynamic response of greatly increased cross-plane thermal conductivity.

Chapter 3: Methods

Heat dissipation and insulation are key components in MEMS fabrication, and both material thermal conductivity and interfacial resistance are fundamental considerations when designing these structures. If thermal conductivity is measured accurately, device composition becomes much simpler and expedite material selection. This information is usually simple to obtain for bulk materials as there are many practices to do so, such as steady-state, laser flash diffusion, transient hot wire, and transient plane source methodologies.

Modern technologies in the semiconductor industry have become miniaturized to the nano- and microscale. Here, large surface-to-volume ratio materials are required, thus media thickness plunged. Thin films are used expansively MEMS, solar technology, micro-, piezo-, and thermoelectrics, all of which require thicknesses spanning from micro to nanometers. In this regime of materials, thermal properties vary from their bulk forms and heat accumulation in small devices becomes much more significant as it can jeopardize operational stability. When using these types of materials, it is up great importance to not only the cross-plane thermal conductivity but its in-plane counterpart with respect to layer dependency. With small sample sizes and the thin condition, conventional methods are not suited to measure temperature and heat fluctuations along the nano- and microscale.

Conventional technologies for measuring thermal conductivity typically cannot be applied for these materials in question as they are physically too large to measure heat transfer across micro and nano length scales [67]. Several decades have been dedicated to overcoming these challenges in measuring thin film thermal conductivity and unique solutions have been demonstrated for use in semiconductor engineering.

Popular in the scientific community, steady-state measurements use temperature sensors deposited on both sides of a film with a heater supplying energy flow on one side only. Being straightforward in principle, the heat flux and temperature changes can be actively monitored in this type of setup. Alongside this, transient methods are used with the widely adopted 3ω being present in many research institutions. This heat transfer quantification technique uses an AC current, at defined frequency ω, to pass through a heater causing a voltage modulation at 3ω, containing the pursued thermal transport information. These measurements require extensive, and often times difficult, sample preparations. Both of these presented techniques call for the deposition of metallic strips of precise dimensions that can only be done with a wide spanning array of micro-fabrication processes.

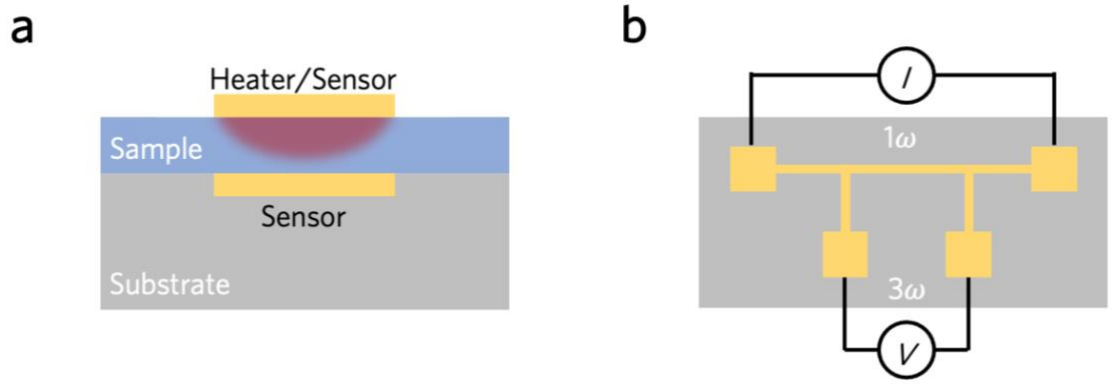

Figure 3.1: Experimental schematics for the a) steady-state thermal measurement and b) the 3ω technique.

3.1 Picosecond Transient Thermoreflectance

Optical thermoreflectance is a data collection technique that measures thermal information of materials with many advantages. Firstly, sample preparation is very simple and does not require exotic equipment. This technique also allows a multitude of

samples to be processed as the measurement is purely optical and no electrical are contacts needed, which is especially difficult to deposit on this scale. This methodology usually requires the sample to be coated with a metal transducer which partakes in a temperature increase from the first "pump" laser. This change in temperature is monitored by a second "probe" laser that is delayed with respect to the pump. This operation allows us to assume that $\Delta R/R=\Delta T/T$ when the change in temperature is small. Furthermore, by modifying the aforementioned delay between pump and probe beams, the temporal response of temperature change prompted from the pump can be observed [68].

Customarily, femtosecond time-domain thermoreflectance (fs-TDTR) uses a Ti:Sapphire laser that operates with a center wavelength usually in the neighborhood of 800 nm with an oscillating repetition rate of roughly 80 MHz. This output source is split into the previously described pump and probe to heat and measure the temperature fluctuations across the sample. The pump beam is restrained based on experimental design with either an electro-optic or acoustic-optic modulator. Thermoreflectance data can then be obtained with a simple detector and unraveled with a lock-in amplifier (LIA). This LIA instrumentation records both in-phase (V_{in}) and out-of-phase (V_{out}) signals which carry separate information. Firstly, V_{in} corresponds to the surface temperature of the sample as it undergoes the laser induced heating and cooling processes. Secondly, the V_{out} data carries the sinusoidal heating of data of the sample at the defined modulation frequency. This data can then be analyzed as V_{in}/V_{out} to fit thermal diffusion models, providing the sought-after thermal information of materials. There is a clear advantage to analyzing the sample response as this ratio in that methodical errors are automatically avoided. Firstly, erroneous signal from non-concentric overlap of the pump and probe beams cancel out as change in both V_{in} and V_{out} take place concurrently. Secondly, this

ratio has no dependance on sample reflectivity or absorptivity nor does it have any dependance on incident laser intensity [69]. Despite these clear advantages in using fs-TDTR, there is a drawback deriving from the characteristic 12.5 ns pulse interval ins Ti:Sapphire oscillating laser. Most materials tend to have a longer relation time than these repeating laser pulses, leading to amassed heat left in the sample that must be considered in data consolidation.

Picosecond transient thermoreflectance (ps-TTR) spectroscopy was developed in this laboratory to perform experiments measuring thermal conductivity without effects from heat accumulation. Figure 3.2 illustrates the optical beam paths for transient thermoreflectance. Here, the main heat source, i.e., the pump laser, is supplied by a picosecond Coherent Talisker (1064 nm, pulse width 15 ps, 200 kHz) and the change in reflectance due to the gold (Au) transducer is recorded via the Coherent Verdi probe laser (532 nm, continuous wave). An acoustic-optical modulator (AOM) based divisor was implemented to reduce the repetition rate to 1 kHz by picking up 1 per 200 pulses. Both pump and probe beams, with spot sizes of 120 and 10 μm ($1/e^2$ diameter), respectively, are colinearly incident on the sample by way of a Mitutoyo 10X IR long working distance objective lens. Here, the size difference between pump and probe beam diameter, along with the sample thickness, guarantee the one-dimensional (1D) heat conduction model to be valid. In this optical table, a polarized beam splitter (PBS) and a quarter waveplate (QWP) are placed before the objective. This is done so that the probe beam passes the QWP twice (incident and reflected) and the loss of probe beam signal through the reflection is minimized. The reflected signal from the probe beam is read by an avalanche photodetector (Hamamatsu C5658, 1GHz bandwidth) and recorded via an oscilloscope (TDS 744A, 2 GS/s sampling rate).

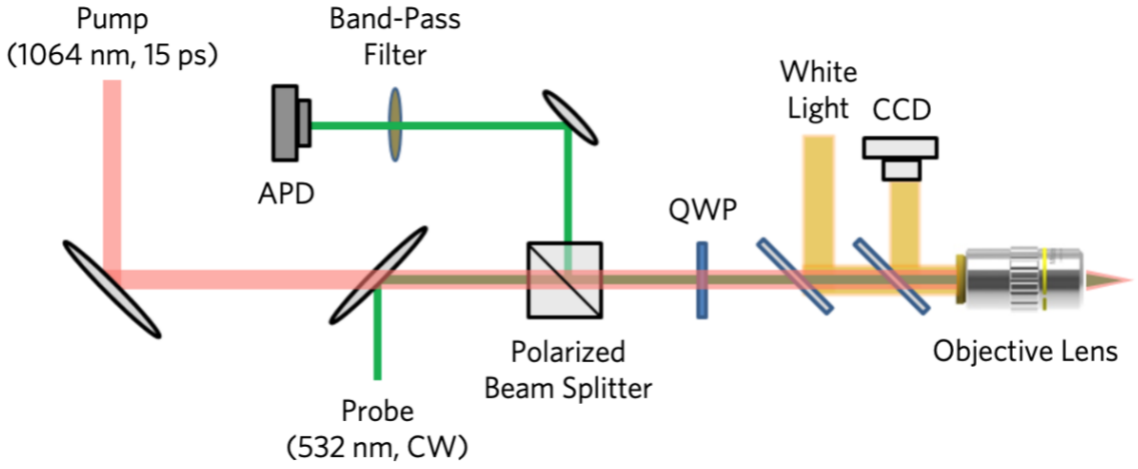

Figure 3.2: Optical beam paths of the ps-TTR measurement system [70].

In comparing fs-TDTR and the developed ps-TTR, there are two distinct advantages in using latter technique for accurate material probing for thermal properties. Firstly, a much simpler optical path can be built as the implementation of a CW laser acting as the probe provides direct time-resolved data via an oscilloscope, rather than using a translation stage. Secondly, heat accumulation in the sample no longer needs to be accounted for as a low repetition rate ensures that complete sample relaxation takes place in between pump laser pulses.

3.2 RAMAN SPECTROSCOPY

Across a wide range of scientific disciplines, Raman spectroscopy is used to probe and identify the vibrational states of materials. The spectroscopic technique uses a CW laser beam to excite a material and induce an emission of photons. This difference between excitation and emission energies correspond to vibrational energies and can be quantified by the equation below.

$$\Delta\nu = \frac{1}{\lambda_0} - \frac{1}{\lambda_1} \tag{3.1}$$

Where, $\Delta\nu$ is Raman shift, λ_0 and λ_1 are the laser wavelength of photon excitation and emission, respectively.

Spectra were obtained using a Renishaw inVia Raman spectrometer. Data was collected with 532 nm excitation wavelength with a 2400 lines/mm grating for 10 seconds, averaged over 3 accumulations on the sample. A long working distance 20X objective produced a 5 μm laser spot size was used to view the thin sample inside the DAC.

3.3 SAMPLE PREPARATION

Thin graphite samples were obtained from a bulk highly order pyrolytic graphite (HOPG) crystal (2D Semiconductors) via micromechanical cleavage with a non-residual semiconductor tape (UltraTape). The sample thickness had some conditions needed to be met in order to meet the requirements the DAC: (1) being able to fit in the 400 μm diameter culet, (2) be thin enough to fit the gasket, (3) Must be thick enough to ignore heat conduction across the HOPG/diamond interface, and (4) have a smooth, reflective surface. Therefore, the exfoliated HOPG was chosen based on these conditions. The sample that met this criterion is 124 μm in its longest diagonal length. The thin HOPG specimen then underwent thermal deposition of a nanometer thickness transducer layer of Au under a pressure of 5×10^{-6} Torr. AFM was then used to measure both the thicknesses of the sample and Au layer, being 4.7 μm and 64 nm, respectively. Both samples and two small rubies were subsequently transferred onto the diamond culet of the DAC with a micro-edge tip. The chamber was then filled with silicon (Si) oil for its natural thermal stability [71] and low probability for unwanted intercalation reactions.

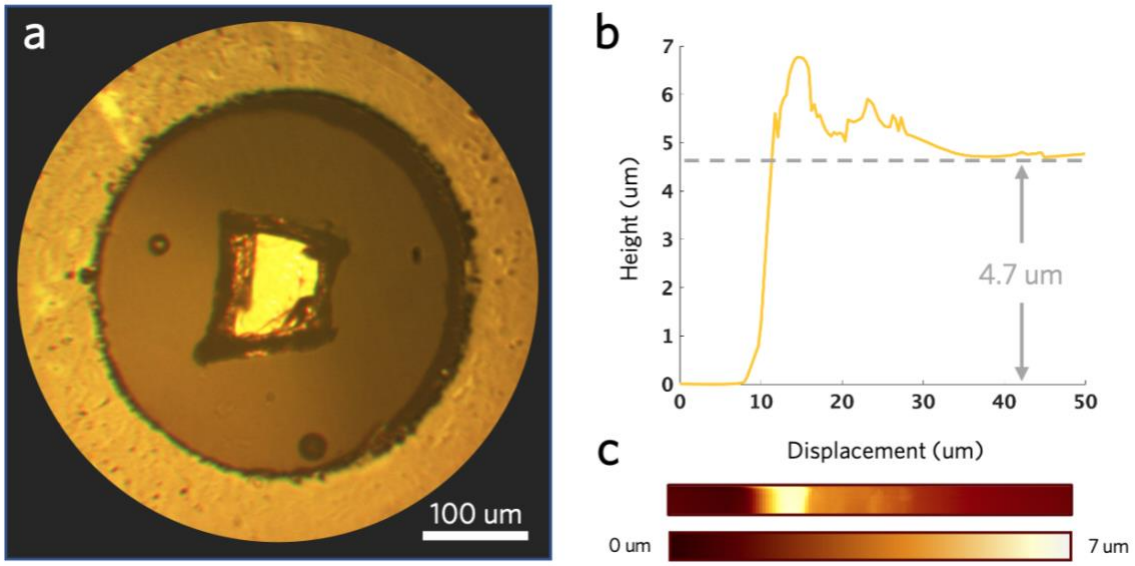

Figure 3.3: a) Optical image of the Au coated HOPG sample in the DAC with two rubies, one below and one to the left. b) AFM tapping data of the bare HOPG specimen with c) the corresponding displacement map.

3.4 Heat Conduction Model

A time-resolved temperature profile used to extract thermal conductivity data was calculated from the following one-dimensional (1D) thermal conduction model.

$$\rho c_p \frac{\partial T}{\partial t} = \kappa \frac{\partial^2 T}{\partial z^2} + \dot{S} \tag{3.2}$$

Where, ρ is density, c_p is specific heat, T is temperature, κ is thermal conductivity and $\dot{S}$ is the heat source from the pump laser. Here, we can quantify the heat source term as a Gaussian laser pulse, which is quantified by the following equation.

$$\dot{S} = I_0(1-r)\exp\left(-\frac{t^2}{\tau^2}\right)\exp(-\alpha z) \tag{3.3}$$

Here, I_0 is peak laser intensity, r is reflectivity (0.979 at 1064 nm), τ is the spectral width of the laser pulse (FWHM, 15 ps), and α is the pump wavelength dependent absorption coefficient of Au (8.22 × 105 cm^{-1} at 1064 nm). Using this information and a pump pulse energy of 800 nJ, the temperature rise can be estimated to be roughly 9 K in the Au layer. Fitting parameters for calculating $\kappa_\perp$ were adapted from [72] for $c_{p,\,Si\ oil}$, [73] for $\kappa_{Si\ oil}$, [74] for $c_{p,\,Au}$, and [75] for $c_{p,\,HOPG}$.

3.5 Uncertainty Analysis

Methods for finding the minimized square difference between experimental and simulated data have been developed extensively by Jiang *et al.* [76]. Alongside this, Yang *et al* [77]. have published methodologies to estimate the uncertainty associated with calculated fitting parameters. A combination of these two techniques was used for this study in maintaining a small uncertainty fitting to the 1D thermal conduction model. Thermal conductivity and interfacial resistance between the transducer layer and sample were extracted from the raw experimental data using an iterative approach to varying time ranges with a least-squared regression fitting, which can be mathematically described below.

$$\psi(U)=\Sigma_{i=1}^{M}\left(R_{exp}(t_i)-f(U,P,t_i)\right)^2 \tag{3.4}$$

Where, $R_{exp}(t_i)$ is the thermoreflectance signal at time t_i, f is the simulated thermoreflectance, U is a column vector of unknown values representing $(\kappa_{HOPG}, R_1, R_2)^T$, and P is a vector with known input values. Moving forward, the gradient of the above equation must zero for the best fit.

$$\Sigma_{i=1}^{M} 2\left(R_{\exp}(t_i)-f(U,P,t_i)\right)\left(\frac{\partial f}{\partial u_j}\right)_{U^0}=0 \tag{3.5}$$

Where, u_j is the j-th component of *U*. First order Taylor expansion at the neighboring point (U^*, P^*) converts this into a matrix structure.

$$J^T(R - F) - J^T J\,(U^* - U^0) - J^T J\,(P^* - P) = 0 \qquad (3.6)$$

Where, $R_{exp} = (R_{exp}(t_1), R_{exp}(t_2), \dots, R_{exp}(t_N))^T$ is the measured thermoreflectance, *F* is the simulated thermoreflectance, J_U and J_P are the Jacobian matrices of the original 1D thermal conduction model. Further expansion of these matrices defines the following.

$$J_U = \begin{pmatrix} \frac{\partial f(t_1)}{\partial u_1} & \cdots & \frac{\partial f(t_1)}{\partial u_l} \\ \vdots & \ddots & \vdots \\ \frac{\partial f(t_N)}{\partial u_1} & \cdots & \frac{\partial f(t_N)}{\partial u_l} \end{pmatrix}_{U_0,P} \quad ; \quad J_P = \begin{pmatrix} \frac{\partial f(t_1)}{\partial p_1} & \cdots & \frac{\partial f(t_1)}{\partial p_m} \\ \vdots & \ddots & \vdots \\ \frac{\partial f(t_N)}{\partial p_1} & \cdots & \frac{\partial f(t_N)}{\partial p_m} \end{pmatrix}_{U_0,P} \qquad (3.7; 3.8)$$

Here, U^* - U^0 can be represented with a linear function, P^* - *P*.

$$U^* - U^0 = (J^T J)^{-1} J^T (R - F) + (J^T J)^{-1} (J^T J)(P^* - P) \qquad (3.9)$$

Performing a covariance operation on both sides of this equation yields the following error propagation formula and carries the desired uncertainty data.

$$\mathrm{var}[U] = J_U^T (J_U^T J_U)^{-1} \mathrm{var}(R_{exp}) J_U (J_U^T J_U)^{-1} + J_U^T J_P (J_U^T J_U)^{-1} \mathrm{var}(P) (J_U^T J_P)^T (J_U^T J_U)^{-1} \qquad (3.10)$$

Furthermore, we define the covariance matrices as follows, with the variances of the unknown parameters being the diagonal elements and the other elements being the covariance itself.

Chapter 4: Results and Discussion

Materials for use in semiconductor processes and devices tend to have a limiting factor in cross-plane thermal conductivity ($\kappa_{\perp}$). Having a device optimized for heat dissipation is key in modern microelectronics. Previous studies have demonstrated quasi-diamond graphitic materials to have largely enhanced thermodynamic activity, however, none have reported quantifiable evidence of the increasing $\kappa_{\perp}$. As previously stated, the phase transformation of dynamics of graphite to diamond is still largely not understood nor measured. Graphene has drawn a mass attention in the scientific community as it highly thermally conductive, measure to be ~4000 $Wm^{-1}K^{-1}$ in a multitude of studies [78]. This value can be further enhanced via strain tuning with studies showing through-plane thermal conductivity ($\kappa_{\parallel}$) to double [79] or even triple [80] in magnitude. Therefore, investigating $\kappa_{\perp}$ is imperative in progressing both the academic research and industrial microelectronics communities.

In this work, graphite measured to be 4.7 μm in thickness was monitored *in-situ* for a diamond transition in a DAC with Raman spectroscopy and ps-TTR up to ~20 GPa. To track the pressure inside of the chamber, ruby florescence was measured with a home-built Raman spectroscope. Naturally, a ruby has a defined peak, coined R_1, at ~694 nm wavelength and experiences a red shift without band softening when strain is applied. Using this value, models developed by Mao *et al.* [81] and Dewaele *et al.* [82] were used to calculate the applied hydrostatic pressure onto the graphite sample by way of Si oil acting as the PTM. Figure 4.1 a) demonstrates this red shift for pressures measured at 5.12, 10.27, and 15.03 GPa. Accordingly, the R_1 peak position was plotted as a function of pressure with both Mao and Dewaele models in Figure 4.1 b). Here, both

approximations are in well agreement with a steady, linear increase of pressure up to 20.28 GPa from ambient.

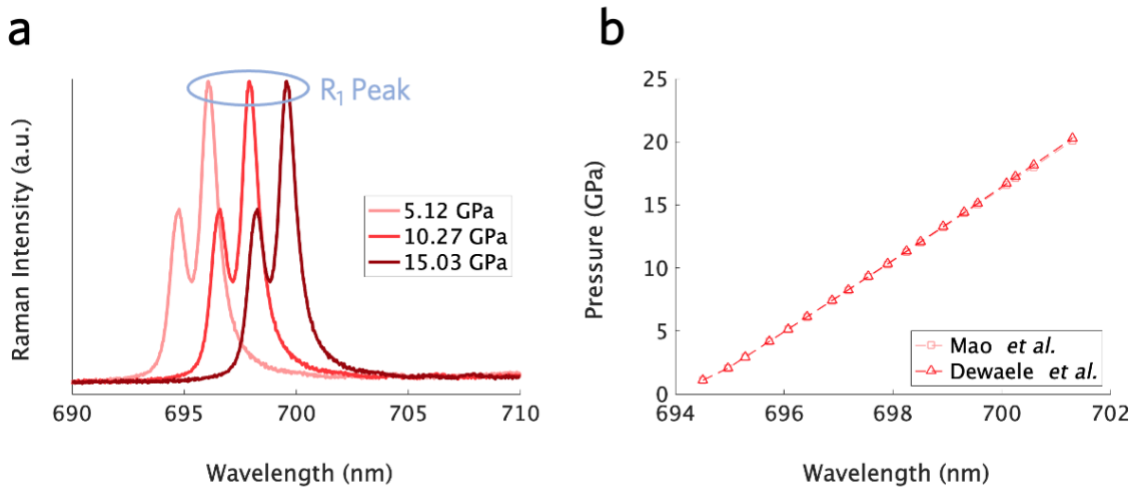

Figure 4.1: a) R_1 peak of ruby florescence at selected pressures and b) calculated hydrostatic pressure in the DAC chamber as a function of R_1 peak shift.

Raman spectroscopy is a great tool for monitoring the *in-situ* transition of graphite to diamond as graphite intrinsically has very active Raman modes that are simple to track. First, the G peak is most prominent in spectra at ~1580 cm^{-1} and is attributed to bond stretching of sp^2 atom pairs. Second, the 2D peak at ~2700 cm^{-1} comes next in distinction as the second order of D (~1360 cm^{-1}), of which is recognized as the highest optical branch from the **K**-A_1' Raman mode [83]. In this study, laser excitation wavelength of 514 nm was used.

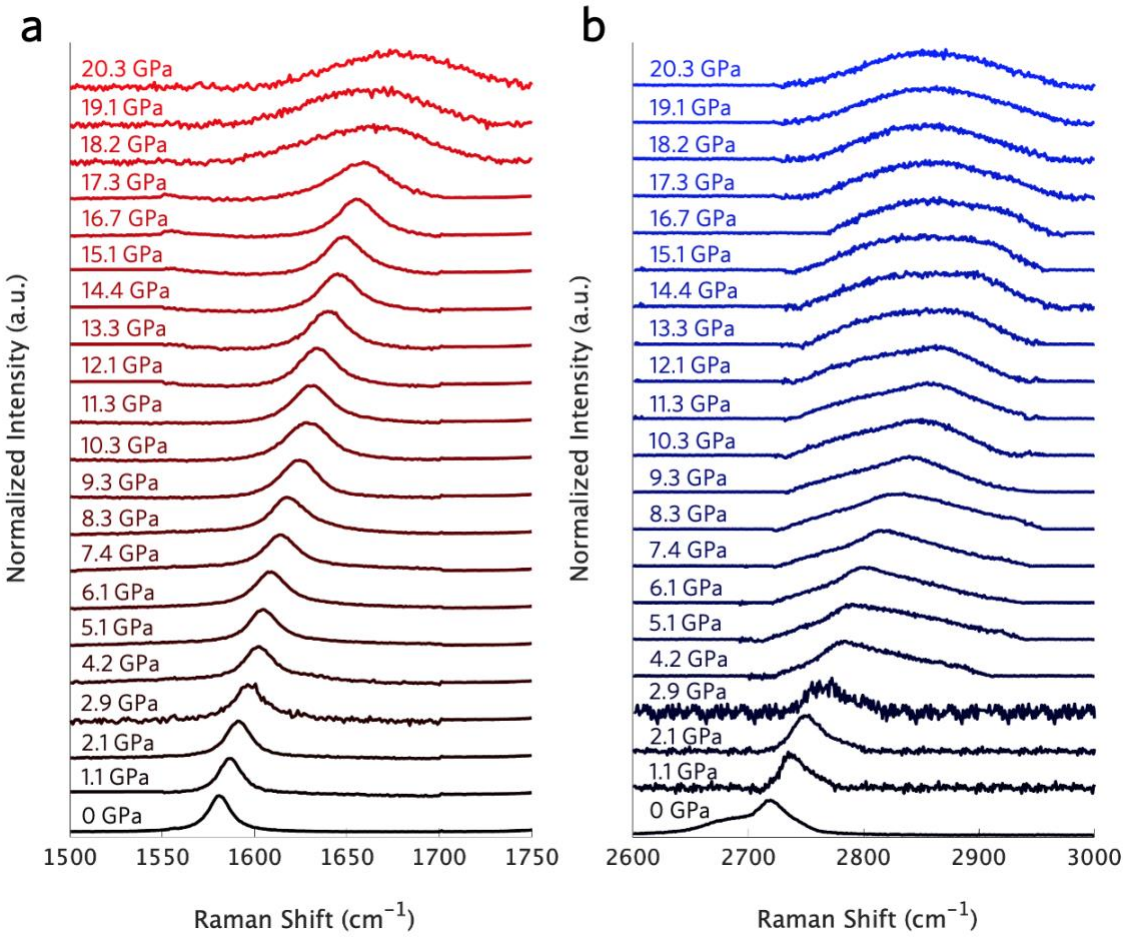

Figure 4.2: Evolution of a) the G and b) 2D peaks as a function of pressure.

Figure 4.2 a) and b) demonstrates a near-linear shift in peak position to higher energy as hydrostatic pressure increases onto the sample. Extreme band softening takes place at between 17 and 18 GPa, the first indication of phase transformation of graphite to a thin diamond film. Lorentzian distribution was used to fit the Raman spectra and peak positions and full width at half maximum (FWHM) were extracted. In comparing from ambient, the FWHM at 18 GPa was measured to increase 56.5 cm^{-1} and 95.4 cm^{-1} for the G and 2D peaks, respectively. Alongside this, the peak positions shift for the same change in pressure was measured to be 83.7 cm^{-1} and 146.7 cm^{-1} for G and 2D,

respectively. Notably, the 2D Raman mode of graphite consists of two peaks that blend together and undergo a dispersion, as shown in Figure 4.3 b).

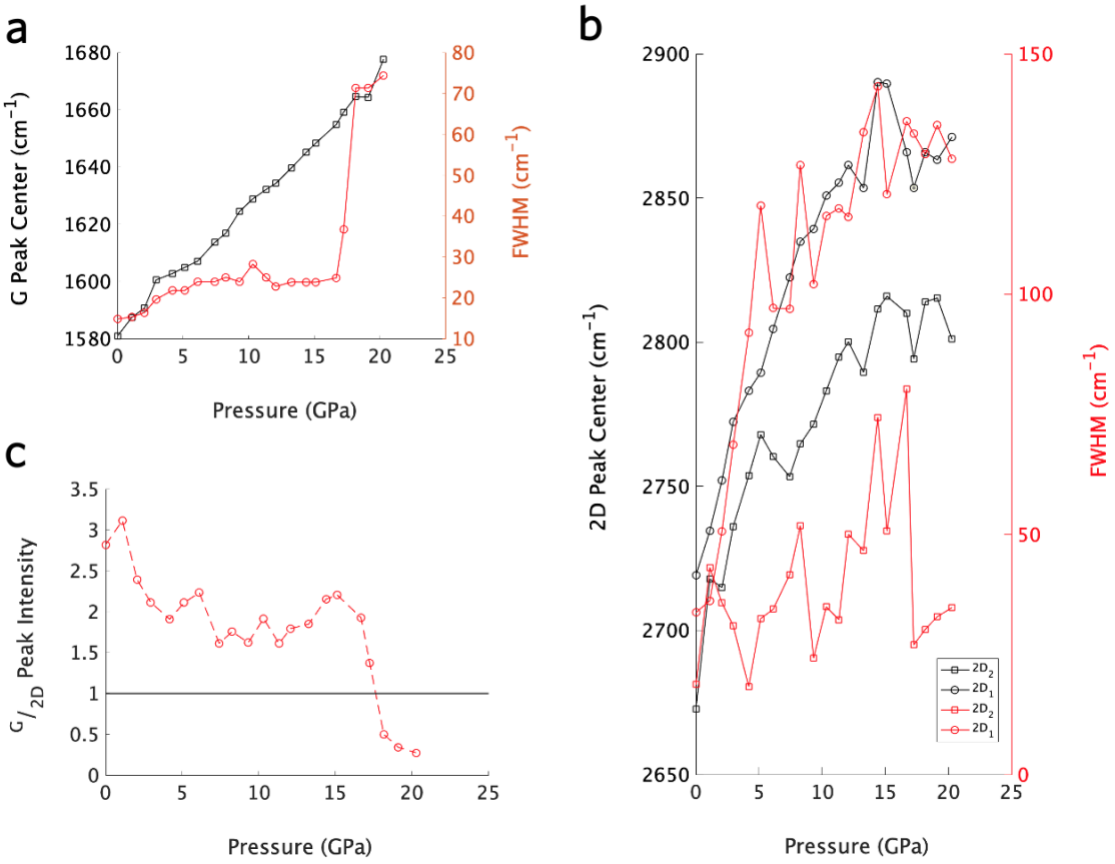

Figure 4.3: Evolution of peak center positions and FWHM values for the a) G and b) 2D peaks, and c) the calculated ratio of normalized peak intensity of active Raman modes of interest.

There is a natural distinction between graphene and graphite in Raman spectroscopic data. It is widely accepted that the ratio of G/2D peak intensities is greater than 1 for bulk graphite samples and less than 1 for graphene. Here, the most profound evidence of a phase transformation is apparent as the flip from graphite indicating a new quasi-diamond material happens in between 17 and 18 GPa of hydrostatic pressure

imposed. This change in normalized peak intensity ratios reinforces the signaling of a phase transformation taking place as the extreme band softening also takes place in the same pressure state.

The next measurement taken was performed using the aforementioned ps-TTR system. Prior to compression in the DAC, the Au coated graphite sample was measured in ambient pressure to be 5.9 ± 0.3 $Wm^{-1}K^{-1}$, which is in agreement with previously reported HOPG samples of similar thicknesses (~5-7 $Wm^{-1}K^{-1}$).

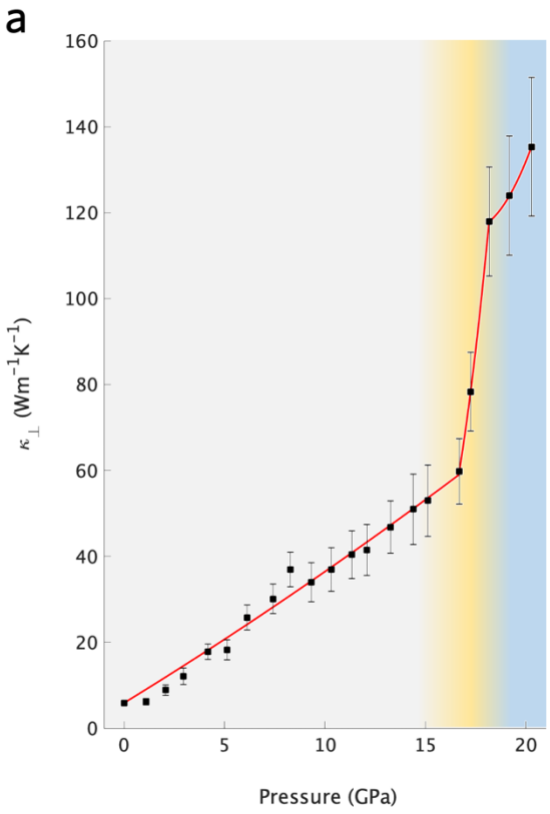

Figure 4.4: a) Extracted $\kappa_\perp$ values of thin HOPG under high compressive strain with the red curve serving as a visual aid

Based on the acquired $\kappa_\perp$ values, we see a drastic increase from ambient with a measured cross-plane thermal conductivity value of 135.3 ± 16 $Wm^{-1}K^{-1}$. Here, we have

demonstrated a substantial increase as the phase transition takes place of ~180% (~22x) the original value under ambient pressure. In Figure 4.4 a), regions of interest are colored with gray corresponding to the original thin HOPG state, gold to the transitional state, and blue to the thin diamond-like film. This large enhancement of $\kappa_{\perp}$ can be attributed to two possible origins: 1) an enhanced phonon contribution to the cross-plane heat dissipation due to a newly modified phonon structure caused by large shrinking of interlayer distance and 2) conversion of vdW to covalent bonds intralayer and the formation of sp^3-hybrid orbitals from the original sp^2. In comparison to literature, origin 2) may be the most dominant as we can estimate interlayer bonding conversion to take ~40-50% of vdW bonding forces based on the MD simulation by Guo *et al.* [84].

Chapter 5: Conclusions and Outlook

This work presents experimental validation of graphite to diamond conversion at ~18 GPa of hydrostatic compression in a DAC for a 4.7 μm thick HOPG sample. Raman spectroscopy was performed *in-situ* to find an extreme band softening of 56.5 cm^{-1} and 95.4 cm^{-1} for the G and 2D peaks, respectively. Furthermore, ps-TTR data measured the cross-plane thermal conductivity to increase ~180% at ~20 GPa post phase transition. Here, we gather the contribution of increased $\kappa_{\perp}$ mainly being contributed to weak interlayer vdW forces being converted into strong covalent bonds and sp^2 electron orbitals translating into sp^3.

This study can be supplemented with theoretical simulations targeting the amount of covalent bonds being formed as the logically, this only takes place currently in the outer layers. Furthermore, a DAC capable of higher pressures can be used to find the limit of $\kappa_{\perp}$ no longer increasing. Once one finds this leveling off limit, it can be implied that all vdW bonds are nonexistent and the sample is populated as sp^3. Finally, highly amorphous sp^3 carbon is easily detectible with Raman spectroscopy with UV excitation, with peaks being separate from the G and 2D bands and easily identifiable when arisen.

Bibliography

1 Stark, A. M. Carbon emissions, energy flow charts for all U.S. states. *Lawrence Livermore National Laboratory,* Retrieved from https://flowcharts.llnl.gov/ (2020 July 28).

2 Hardwick, D. A. The mechanical properties of thin films: a review. *Thin Solid Films* **154**, 109-124 (1987).

3 Kraft, O., & Nix., W. D. Measurement of the lattice thermal expansion coefficients of thin metal films on substrates. *J. Appl. Phys.* **83**, 3035 (1998).

4 Schmidt, A. J., Cheaito, R., & Chiesa M. Characterization of thin metal films via frequency-domain thermoreflectance. *J. Appl. Phys.* **107**, 024908 (2010).

5 R. C. Dynes, V. Narayanamurti, & J. P. Garno. Direct Measurement of Quasiparticle-Lifetime Broadening in a Strong Coupled Superconductor. *Phys. Rev. Lett.* **41**, 1509 (1978).

6 Goyal, V., Tewelebhan, D., & Balandin, A. A. Mechanically-exfoliated stack of thin films of Bi_2Te_3 topological insulators with enhanced thermoelectric performance. *Appl. Phys. Lett.* **87**, 133117 (2010).

7 Liu, W., & Asheghi, M. Thermal Conductivity Measurements of Ultra-Thin Single Crystal Silicon Layers. *J. Heat Transfer* **128**(1), 75-83 (2006).

8 Luo, Z., *et al.*, Large Enhancement of Thermal Conductivity and Lorenz Number in Topological Insulator Thin Films. *ACS Nano.* **12**, 1120-1127 (2018).

9 Avery, A. D., *et al.*, Thermopower and resistivity in ferromagnetic thin films near room temperature. *Phys. Rev. B.* **83**, 100401 (2011).

10 Mondal S., & Barman, A. Laser Controlled Spin Dynamics of Ferromagnetic Thin Film from Femtosecond to Nanosecond Timescale. *Phys. Rev. Appl.* **10**, 054037 (2018).

11 Hseih, D., *et al.*, A topological Dirac insulator in a quantum spin Hall phase. *Nature* **452**, 970-974 (2008).

12 Geim, A. K., & Grigorieva, I. V., Van der Waals heterostructures. *Nature* **499**, 419-425 (2013).

13 El-Kady, M. F., Strong, V., Dubin, S. & Kaner, R. B. Laser scribing of high-performance and flexible graphene-based electrochemical capacitors. *Science* **335**, 1326-1330 (2012).

14 Miao, X. *et al.* High efficiency graphene solar cells by chemical doping. *Nano Lett.* **12**, 2745-2750 (2012).

15 Chung, D. D. L., Review Graphite. *J. of Mater. Sci.* **37**, 1475-1489 (2002).

16 Novoselov, K. S., *et al.*, Electric field effect in atomically thin carbon films. *Science* **306**, 666-609 (2004).

17 Hull, A. W. A new method of x-ray crystal analysis. *Phys. Rev.*, **10**, 661-696 (1917).

18 Bernal, J. D., & Bragg, W. L. The structure of graphite. *Proc R. Soc. Lond. A.* **740**, 749-773 (1924).

19 Kim, T. I., Park, I.-J., & Choi, S.-Y. Synthesis of ultrathin metal nanowires with chemically exfoliated tungsten disulfide nanosheets. *Nano Lett.*, **20**, 3740-3946 (2020).
20 Anthony, J. W., *et al.*, Graphite. *Handbook of References Mineralogy*, **1**, 2001-2005 (1990).
21 Delhaes, P., Polymorphism of carbon. Gordon and Breach, **1**, 1-24 (2000).
22 Pierson, H. O., Handbook of carbon, graphite, diamond, and fullerenes: properties, processing, and applications. *Noyes Publications*, **1**, 40-41 (2012).
23 Pek, J., & Verner T., Finite-difference modeling of magnetotelluric fields in two-dimensional anisotropic media. *Geophys. J. Int.*, **128**, 505-521 (1997).
24 Nguyen, E. P. *et al.* Electronic tuning of 2D MoS_2 through surface functionalization. *Adv. Mater.* **27**, 6225-6229 (2015).
25 Ataca, C. & Ciraci, S. Functionalization of single-layer MoS_2 honeycomb structures. *J. Phys. Chem. C* **115**, 13303-13311 (2011).
26 Nan, H. *et al.* Strong photoluminescence enhancement of MoS_2 through defect engineering and oxygen bonding. *ACS Nano* **8**, 5738-5745 (2014).
27 Islam, M. R. *et al.* Tuning the electrical property via defect engineering of single layer MoS_2 by oxygen plasma. *Nanoscale* **6**, 10033-10039 (2014).
28 Qiu, H. *et al.* Hopping transport through defect-induced localized states in molybdenum disulphide. *Nat. Commun.* **4** (2013).
29 Briggs, N., *et al.*, Epitaxial graphene/silicon carbide intercalation: a minireview on graphene modulation and unique 2D materials. *Nanoscale* **11**, 15440-15447 (2019).
30 Nakano S., *et al.*, Pressure-induced intercalation of alcohol molecules into a layered titanate. *Chem. Mater.* **8**, 2044-2046 (1998).
31 Zhang, X., Shyy, W., & Sastry, A. M., Numerical simulation of intercalation-induced stress in Li-ion battery electrode particles. *J. Electrochem. Soc.* **154**, A910 (2007).
32 Sachs, B. *et al.* Doping mechanisms in graphene-MoS_2 hybrids. *Appl. Phys. Lett.* **103**, 251607 (2013).
33 Laskar, M. R. *et al.* P-type doping of MoS_2 thin films using Nb. *Appl. Phys. Lett.* **104**, 092104 (2014).
34 Morgan Stewart, H., Shevlin, S. A., Catlow, C. R. A. & Guo, Z. X. Compressive straining of bilayer phosphorene leads to extraordinary electron mobility at a new conduction band edge. *Nano Lett.* **15**, 2006-2010 (2015).
35 Peelaers, H. & Van de Walle, C. G. Effects of strain on band structure and effective masses in MoS 2. *Phys. Rev. B* **86**, 241401 (2012).
36 Quereda, J. *et al.* Strong modulation of optical properties in black phosphorus through strain-engineered rippling. *Nano Lett.* **16**, 2931-2937 (2016).
37 Desai, S. B. *et al.* Strain-induced indirect to direct bandgap transition in multilayer WSe_2. *Nano Lett.* **14**, 4592-4597 (2014).

38 Roldán, R., Castellanos-Gomez, A., Cappelluti, E. & Guinea, F. Strain engineering in semiconducting two-dimensional crystals. *J. Phys.: Condens. Matter* **27**, 313201 (2015).
39 Mohiuddin, T. *et al.* Uniaxial strain in graphene by Raman spectroscopy: G peak splitting, Grüneisen parameters, and sample orientation. *Phys. Rev. B.* **79**, 205433 (2009).
40 Jie, W., *et al.*, Ferroelectric polarization effects on the transport properties of graphene/PMN-PT field effect transistors. *J. Phys. Chem. C.* **117**, 13747-13752 (2013).
41 Hui, Y. Y. *et al.* Exceptional tunability of band energy in a compressively strained trilayer MoS_2 sheet. *ACS Nano* **7**, 7126-7131 (2013).
42 Manzeli, S., Allain, A., Ghadimi, A. & Kis, A. Piezoresistivity and strain-induced band gap tuning in atomically thin MoS_2. *Nano Lett.* **15**, 5330-5335 (2015).
43 Lloyd, D. *et al.* Band gap engineering with ultralarge biaxial strains in suspended monolayer MoS2. *Nano Lett.* **16**, 5836-5841 (2016).
44 Nayak, A. P. *et al.* Pressure-induced semiconducting to metallic transition in multilayered molybdenum disulphide. *Nat. Commun.* **5** (2014).
45 Hsieh, W.-P., Chen, B., Li, J., Keblinski, P. & Cahill, D. G. Pressure tuning of the thermal conductivity of the layered muscovite crystal. *Phys. Rev. B* **80**, 180302 (2009).
46 Conley, H. J. *et al.* Bandgap engineering of strained monolayer and bilayer MoS_2. *Nano Lett.* **13**, 3626-3630 (2013).
47 Bertolazzi, S., Brivio, J. & Kis, A. Stretching and breaking of ultrathin MoS_2. *ACS Nano* **5**, 9703-9709 (2011).
48 Jayaraman, A. Diamond anvil cell and high-pressure physical investigations. *Rev. Mod. Phys.* **55**, 65 (1983).
49 Mao, H., Xu, J.-A. & Bell, P. Calibration of the ruby pressure gauge to 800 kbar under quasi-hydrostatic conditions. *Journal of Geophysical Research: Solid Earth* **91**, 4673-4676 (1986).
50 Dewaele, A., Torrent, M., Loubeyre, P. & Mezouar, M. Compression curves of transition metals in the Mbar range: Experiments and projector augmented-wave calculations. *Phys. Rev. B* **78**, 104102 (2008).
51 Tsvetkov, N., *et al.* Accelerated Oxygen Exchange Kinetics on $Nd_2NiO_{4+\delta}$ Thin Films with Tensile Strain along *c*-Axis. *ACS Nano* **9**, 1613-1621 (2015).
52 Xue, D.-J., *et al.* Regulating strain in perovskite thin films through charge-transport layers. *Nat. Commun.* **11**, 1514 (2020).
53 Elias, D. C., *et al.*, Control of graphene's properties by reversible hydrogenation: evidence of graphene. *Science*, **323,** 610-613 (2009).
54 Sofo, J. O., Chaudhari, A. S., Barber, G. D., Graphane: A two-dimensional hydrocarbon. *Phys. Rev. B.*, **75**, 153401 (2007).
55 Nair, R. R., *et al.*, Fluorographene: a two-dimensional counterpart to Teflon, *Small* **24**, 2877-2884, (2010).

56 Robinson, J. T., *et al.*, Properties of Flourinated Graphene Films, *Nano Lett.*, **8**, 3001-3005 (2010).
57 Zboril, R., *et. al.*, Graphene Flouride: A Stable Stoichiometric Graphene Derivative and its Chemical Conversion to Graphene, *Small*, **24** 2885-2891 (2010).
58 Mathkar, A., *et al.*, Enhanced Photocatalytic Hydrogen Production over Graphene Oxide-Cadmium Sulfide Nanocomposite Under Visible Light Irradiation, *J. Phys. Chem. Lett.*, **8,** 986-991 (2012).
59 Nicolle, J., *et al.*, Pressure Mediated Doping in Graphene, *Nano Lett.*, **11**, 3564-3568 (2011).
60 Zhou, S. Y., *et al.* Substrate-induced bandgap opening in epitaxial graphene, *Nat. Mater.*, **6,** 770-775 (2007).
61 Sung, J., Graphite to diamond transition under high pressure: A kinetics approach, *J. Mater. Sci.*, **35,** 6041-6054 (2000).
62 Tian, F., *et al.*, Superhard F-carbon predicted by *ad initio* particle-swarm optimization methodology, *J. Phys.: Condens. Matter.*, **24,** 165504 (2012).
63 Tateyama, Y., *et al.*, Constant-pressure first-principles studies on the transition states of the graphite-diamond transformation, *Phys. Rev. B.*, **54,** 14994 (1996).
64 Sluiter, M. H. F., & Kawazoe, Y., Cluster expansion method for adsorption: Application to hydrogen chemisorption on graphene, *Phys Rev. B.*, **68**, 085410 (2003).
65 Lin, Y., Ding, F., & Yakobson., B. I., Hydrogen storage by spillover on graphene as a phase nucleation process, *Phys. Rev. B.*, **78**, 041402 (2008).
66 Luo, D., *et al.*, Ultrafast formation of transient 2D diamond-like structure in twisted bilayer graphene, *Phys. Rev. B.*, **102**, 155431 (2020).
67 Zhao, D., *et al.*, Measurement techniques for thermal conductivity and interfacial thermal conductance of bulk and thin film materials, *J. Elec. Pack.*, **138,** 040802 (2016).
68 Cahill, D. G., Analysis of heat flow in layered structures for time-domain thermoreflectance, *Rev. Sci. Instrum.*, **75,** 5119-5112 (2004).
69 Feser, J. P., & Cahill, D. G., Probing anisotropic heat transport using time-domain thermoreflectance with offset laser spots, *Rev. Sci. Instrum.*, **83**, 104901 (2012).
70 Jeong, J., *et al.*, Picosecond transient thermoreflectance for thermal conductivity characterization, *Nanosc. Microsc. Therm.*, **3,** 211-221 (2018).
71 Moretto, H.-H., Schulze, M., & Wagner, G., Silicones, *Ullmann's Encyclopedia of Industrial Chemistry, (Ed.)* (2000).
72 Hohensee, G. T. *Using high pressure to study thermal transport and phonon scattering mechanisms*. (University of Illinois at Urbana-Champaign, 2015).
73 Hsieh, W.-P. Thermal conductivity of methanol-ethanol mixture and silicone oil at high pressures. *J. Appl. Phys.* **117**, 235901 (2015).
74 Kusaba, K. & Kikegawa, T. Debye temperature of gold under high pressure determined by X-ray powder diffraction method. *Solid State Commun.* **149**, 371-374 (2009).

75 Kuang, Y., Lindsay, L., & Huang, B., Unusual enhancement in intrinsic thermal conductivity of multilayer graphene by compressive strains, *Nano Lett.* **15,** 6121-6127 (2015).
76 Jiang, P., Qian, X., Gu, X. & Yang, R. Probing Anisotropic Thermal Conductivity of Transition Metal Dichalcogenides MX2 (M = Mo, W and X = S, Se) using Time‐Domain Thermoreflectance. *Adv. Mater.* **29** (2017).
77 Yang, J., Ziade, E. & Schmidt, A. J. Uncertainty analysis of thermoreflectance measurements. *Rev. Sci. Instrum.* **87**, 014901 (2016).
78 Ghosh, S., *et al.*, Extremely high thermal conductivity of graphene: prospects for thermal management application in nanoelectronic circuits, *Appl. Phys. Lett.*, **92**, 151911 (2008).
79 Pereira, L. F. C., & Donadio, D., Divergence of the thermal conductivity in uniaxially strained graphene, *Phys. Rev. B.*, **87**, 125424 (2013).
80 Guo, M., *et al.*, Experimental measurements on the thermal conductivity of strained monolayer graphene, *Carbon*, **157**, 185-190 (2020).
81 Mao, H. K., & Bell, P. M., High pressure physics: The 1megabar mark on the ruby R_1 static pressure scale, *Science*, **191**, 851-852 (1976).
82 Dewaele, A., Torrent, M., Loubeyre, P. & Mezouar, M. Compression curves of transition metals in the Mbar range: Experiments and projector augmented-wave calculations. *Phys. Rev. B* **78**, 104102 (2008).
83 Ferrari, A. C., Raman spectroscopy of graphene and graphite: Disorder, electron-phonon coupling, doping and nonadiabadic effects, *Solid State Commun*, **147**, 47-57 (2007).
84 Guo, T., *et al.*, Tuning the thermal conductivity of multi-layer graphene with interlayer bonding and tensile strain, *Appl. Phys. A.*, **120**, 1275-1281 (2015).